HHS Public Access

Author manuscript

Nano Res. Author manuscript; available in PMC 2023 April 01.

Published in final edited form as:

Nano Res. 2022 April ; 15(4): 3409–3421. doi:10.1007/s12274-021-3947-1.

Modeling the gene delivery process of the needle array-based tissue nanotransfection

Zhigang Li[1,2,§], **Yi Xuan**[1,2,§,✉], **Subhadip Ghatak**[1], **Poornachander R. Guda**[1], **Sashwati Roy**[1], **Chandan K. Sen**[1,2,✉]

[1]Indiana Center for Regenerative Medicine and Engineering, Indiana University Health Comprehensive Wound Center, Department of Surgery, Indiana University School of Medicine, Indianapolis, IN 46202, USA

[2]Birck Nanotechnology Center and Weldon School of Biomedical Engineering, Purdue University, West Lafayette, IN 47907, USA

Abstract

Hollow needle array-based tissue nanotransfection (TNT) presents an *in vivo* transfection approach that directly translocate exogeneous genes to target tissues by using electric pulses. In this work, the gene delivery process of TNT was simulated and experimentally validated. We adopted the asymptotic method and cell-array-based model to investigate the electroporation behaviors of cells within the skin structure. The distribution of nonuniform electric field across the skin results in various electroporation behavior for each cell. Cells underneath the hollow microchannels of the needle exhibited the highest total pore numbers compared to others due to the stronger localized electric field. The percentage of electroporated cells within the skin structure, with pore radius over 10 nm, increases from 25% to 82% as the applied voltage increases from 100 to 150 V/mm. Furthermore, the gene delivery behavior across the skin tissue was investigated through the multilayer-stack-based model. The delivery distance increased nonlinearly as the applied voltage and pulse number increased, which mainly depends on the diffusion characteristics and electric conductivity of each layer. It was also found that the skin is required to be exfoliated prior to the TNT procedure to enhance the delivery depth. This work provides the foundation for transition from the study of murine skin to translation use in large animals and human settings.

Keywords

tissue nanotransfection; silicon needle array; hollow needle array; electroporation; electrophoresis; gene delivery

Address correspondence to: Yi Xuan, xuan@iu.edu; Chandan K. Sen, cksen@iu.edu.
§Zhigang Li and Yi Xuan contributed equally to this work.

Electronic Supplementary Material: Supplementary material (free energy of pores on the cell membrane; the drift velocity; the value of transmembrane voltage; the flow field of the cell array-based model; the total amount of transported molecules; the mobility and effective charge of molecules species; partition factor and hindrance factor; the multilayer stack-based delivery model; parameters used in the theoretical models; supplementary Figs S1–S8 and Tables S1–S3) is available in the online version of this article at https://doi.org/10.1007/s12274-021-3947-1.

1 Introduction

Tissue nanotransfection (TNT) is an emerging approach in the field of regenerative medicine that enables non-viral direct reprogramming of terminally differentiated cells to another type *in vivo* [1–4]. During the TNT procedure, by applying electric pulses between the nanofabricated chip and the target tissue or skin, reprogramming factors can be delivered to the target tissue cells through the mechanism of electroporation and electrophoresis. Such a process is considered superior compared to traditional cell reprogramming techniques by circumventing the complex lab operations, safety concerns of virus vectors, and low delivery efficiency [5–9]. In 2017, nanoporous chip-based TNT has successfully demonstrated that skin can be reprogrammed into vascular cells and neuron cells in the mouse model [1]. Later, the hollow needle array-based TNT chip was fabricated and tested on mouse skin to investigate the cutaneous wound healing because of its improved gene delivery efficiency [2].

Electroporation, a physical method to enhance cell membrane permeability via external electric pulses [10–12], has been widely investigated in terms of both theories and experiments in the past years [10, 13–19]. These reports found that when an electric field is applied on cells, the thermal fluctuation introduced hydrophobic pores that can evolve into larger hydrophilic pores on the cell membrane by rearranging polar molecules in the phospholipid bilayer to minimize free energy. These electroporated pores allow the ions and molecules to be transported into or out of the cells, enabling medical applications such as DNA electrotransfer [20], electrochemotherapy [21], drug delivery [22], therapeutic healing [1, 14, 17–19], DNA vaccination [23, 24], sampling target cells for monitoring [25–27], industrial applications in food processing [28, 29], and cell inactivation [30]. Moreover, electroporation method exhibits a simple and efficient way compared with other membrane-disruption based methods such as mechanical methods by physically puncturing [31] or deformation in microfluidic channel [32], and thermal heating by laser [33] as well as nanocarrier-based delivery through biological endocytosis and fusion [34, 35]. However, it has the limitation of requiring high voltage, which can potentially damage cells irreversibly, and results in difficulties in controlling drug doses for cells. To overcome this hurdle, various micro/nano scale electroporation platforms were proposed. With the integration of microfluidic concepts, microelectrode array devices were designed to achieve localized electroporation at a single cell level with high-throughput ability, which can significantly decrease the applied voltage and improve transfection efficiency [36–39]. Moreover, the localized electric field can be further enhanced with nanomaterials such as the nanotube [40], nanopillar [41], nanostraw [25, 26], and nanochannel [1, 42]. Recently, needle array electrode with chip size was proposed for drug delivery and gene vaccination for skin tissue [43, 44]. Hence, miniaturization of the device sizes plays an important role in facilitating and expanding electroporation-based medical applications.

The investigations on the intriguing electroporation-based processes have evolved from single cells to tissues, and to organs, which renders numerous challenges for miniaturizing devices to realize practical *in vivo* applications. The electroporation behavior on tissue is complex compared with a single cell. For example, skin, composed of epidermis, dermis, and hypodermis, has a complex cellular environment and skin structures that vary across sex,

age, individual, and animal species [45–47], significantly affecting the delivery process and the transfection outcome. Even though, *in vivo* electroporation on human skin xenografted onto immunodeficient nude mice has been reported [48], however, it might be difficult to use it in clinical applications due to its bulky caliper-type electrodes. The needle array-based electrode for electroporation was also proposed for drug delivery and gene vaccination for skin tissue, but the needle arrays mainly acted as the electrode [43, 44]. Nanofabricated chip-based TNT approach has been proved to be an efficient, fast, and determined gene delivery approach based on non-virus mediated vector [1–4]. However, prior to clinical applications for human, TNT parameters such as needle design, voltage amplitude, and pulse duration must be optimized for a safe operation and high efficiency. Theoretical modeling is an alternative approach to understanding molecules delivery mechanisms and optimizing TNT parameters prior to preclinical models on pigs and practical applications for humans [10–19].

Compared to our previous works [1, 2], this work aims to theoretically establish a physical model to describe the gene delivery process on the complex skin structure via hollow needle array-based TNT chips. Our prior works did not consider the coexisting influences of the electroporation and electrophoresis contributions in the gene delivery process. Additionally, this work investigates the optimal voltage for TNT process that balances both the safety regulations of applied voltage and gene delivery efficiency through the combination of simulation and experiment.

In this work, we simulated and visualized the gene delivery progress for TNT at the single cell scale by considering electroporation and electrophoresis. Electroporation behaviors of cells located at different positions were discussed in terms of electric field distribution, transmembrane voltage (TMV), pore numbers, pore size, and pore area ratio. The electrophoresis behaviors such as delivery distance, DNA flow flux, and DNA concentration profile were determined to study the factors affecting the delivery efficiency. The voltage effect was also discussed to find optimal parameters to improve the delivery efficiency. *In vivo* TNT on a mouse model by using Si hollow needle array was conducted to validate the simulation results from both the cell-array-based model and the multilayer-stack-based model. This work paves the way to transition from the mouse model to clinical applications for human usage.

2 Experimental

2.1 Fabrication method of the TNT chip

The TNT chip was fabricated out of a double side polished 4-inch Si (100) wafer with standard semiconductor process (Fig. S7 in the Electronic Supplementary Material (ESM)). The fabrication started with spin-coating a ~ 50 μm thick SU-8 3050 photoresist on the backside of the wafer, and patterning a hole array (diameter = 30 μm, spacing = 150 μm) using a direct laser writer (Heidelberg MLA 150). Then, the wafer was etched ~ 450 μm deep by Bosch process (deep Si etching, Plasma-Therm, Versaline). The procedure proceeded with removing the residue SU8, spin-coating SPR 220-7.0 photoresist on the frontside of the wafer and patterning a donut-shape array with precise backside alignment, followed by deep Si etching to form the hollow microneedle array. Deposit a thin SiO_2

film on the frontside of the wafer by plasma enhanced chemical vapor deposition (PECVD) system (Plasma-Therm, Vision 310) to shrink the bore size to the target value. Finally, mount the fabricated TNT chip on a plastic drug reservoir for TNT procedure usage using polydimethylsiloxane (PDMS). Detailed information of this fabrication methods was reported in our previous work [4].

2.2 Numerical implementation of the simulation

The simulation in this work was implemented by coupling the asymptotic model of electroporation and governing equations of molecules transport with the finite element method through the commercial software COMSOL™ [49]. The calculation domain included both the needle array and the cellular architecture in a periodic region to mimic the tissue layer. The cell-to-cell distance was set to 1.43 μm resulting in a porosity of ~ 0.23 in the skin model, which was close to the experimental measurement and within the reported porosity range of tissue cells [50]. To allow the flow of the plasmid solution, half of the cell-to-cell distance was chosen as the gap distance between the needle and the skin region in the simulation. The influence of the gap distance was neglected since it is weak as pointed out in the reference [42]. The initial conditions assumed that plasmid DNA (pDNA) solution was prefilled in the needle array and the pore density was zero. The electric pulse was applied across the tissue and the needle array by setting the upper side of the needle array as ground and bottom of tissue with the positive potential. At each time step, the electric potential field was solved in calculation domain to obtain the transmembrane voltage on the cell membrane, based on which the asymptotic method gave the solutions of the local pore density, pore radius distribution, as well as the membrane resistance due to the formed pores at each discretized patch on the membrane. At the same time, the molecules transport was calculated by solving the Nernst–Planck equation and the flow velocity field to observe the concentration distribution of the molecules within the tissue. Different from the cell-array-based delivery model, no cell electroporation information was needed in the simulation with multilayer-stack-based delivery model. Thus, it only needed to solve the electric field distribution, Nernst–Planck equation and the porous flow equation as given in the SI H in the ESM.

2.3 Animals

Male C57BL/6 mice (aged 8–12 weeks) were obtained from Jackson Laboratory. All animal procedures were conducted following the Institutional Animal Care and Use Committee (IACUC) guidelines. The animal study protocol was approved by the IACUC at Indiana University (protocol # 18047).

2.4 DNA plasmid preparation

Mock (empty vector) and *Ascl1* plasmids were prepared using a plasmid DNA purification kit (ZymoPURE II Plasmid Midiprep Kit, category No. D4201) as described previously [51]. DNA concentrations were obtained from Nanodrop 2000c Spectrophotemeter (Thermoscientific).

2.5 Immunohistochemistry (IHC) and microscopy

Immunohistochemistry was performed as described previously [52]. Immunostainings of green fluorescent protein (GFP, Abcam, ab13970; 1:500) was performed on cryosections of skin sample post-TNT. Briefly, the sections blocked with 10% normal goat serum, and incubated with specific antibodies overnight at 4 °C. Signal was visualized by subsequent incubation with fluorescence-tagged appropriate secondary antibodies (Alexa 488-tagged α-chicken, 1:200) and counter stained with 4',6-diamidino-2-phenylindole (DAPI). Images were captured by microscope using Axio Scan.Z1 (Zeiss, Germany).

2.6 Laser capture microdissection of the epidermis and dermis

Laser capture microdissection was performed using a laser microdissection system from Palm Technologies (Bernreid, Germany) containing a Palm MicroBeam and RoboStage for high-throughput sample collection and a Palm RoboMover (Palm Robo software, Version 2.2) as described previously [53]. For epidermal laser capture microdissection (LCM), sections were stained with hematoxylin for 30 s, subsequently washed with diethyl pyrocarbonate (DEPC)-H_2O and dehydrated in ethanol. The epidermis was identified based on the histology. Epidermal tissue elements were typically cut and captured under a 20× ocular lens. Samples were catapulted into 25 μl of cell lysis buffer (Invitrogen). Approximately 100,000 μm^2 of tissue area was captured into each cap and the extract was then held at −80 °C for further analyses [52].

2.7 Quantitative real-time PCR

For determination of mRNA expression of *Ascl1*, quantified by real-time or quantitative (Q)PCR assay was performed using the double-stranded DNA binding dye SYBR Green-I [2, 54].

2.8 Statistical analysis

GraphPad Prism (GraphPad Software) v8.0 was used for statistical analyses. No statistical methods were used to predetermine the sample size. Statistical analysis between multiple groups were performed using one-way analysis of variance with the post-hoc Bonferroni multiple comparison test. Statistical analysis between two groups were performed using unpaired Student's *t*-tests. $P < 0.05$ was considered statistically significant. Significance levels and exact *P* values were indicated in all relevant figures. Data were assumed to be normally distributed for all analyses conducted. Data for independent experiments were presented as means ± standard error of the mean (SEM) unless otherwise stated.

3 Results and discussion

3.1 The needle array-based TNT approach

Silicon needle array based drug delivery systems are well known for their advantages of mass production with standard semiconductor process [55–57], suitable mechanical strength [56, 57], and biological compatibility [58]. As depicted in Fig. 1(a), the needle array-based TNT approach relies on three important factors, reprograming factors, a TNT chip, and a power system providing electric pulses. A variety of reprograming factors can be selected

for tissue nanotransfection or other specific purposes depending on if the molecules are positive or negative carriers. Negatively charged pDNA was used in this work.

Figure 1(a) schematically presents a typical TNT chip mounted with a reservoir on the backside, where the reservoir serves as a storage for gene solution, and a schematic design of the TNT chip is given in Fig. 1(b), showing the Si hollow needle array with flat tip. For a typical TNT procedure, the reservoir mounted chip is placed on an exfoliated skin, and then a series of electric pulses is applied to deliver the genes from the reservoir to the target tissue through hollow microchannels as shown in Fig. 1(c). The TNT chip was fabricated by using the standard semiconductor process that enables low-cost mass production [4]. The process mainly involves lithography and deep silicon etching which is detailed in the Methods section. Figures 1(d)–1(f) show the typical SEM and optical images of the fabricated TNT chip. The needle has a spacing of 150 μm, a length of ~ 125 μm, an inner diameter of ~ 4 μm at the tip, and an outer diameter of ~ 55 μm after coated with a thin layer of SiO_2 to insulate the surface of the silicon hollow needle array. The needle array is connected to the drug reservoir on the backside of the chip via a pathway with a bore diameter of ~ 30 μm (Fig. 1(f)). The total height of the TNT chip is ~ 525 μm.

3.2 Theoretical model of the needle array-based TNT approach

Theoretical studies on the electroporation process of a single cell or a few cells have been implemented and revealed the mechanisms of pore formation and evolution on the cell membrane [10–12]. Usually, it requires a large computational cost when calculating time-dependent pore evolution, for instance, pore radius and pore area ratio were usually calculated through Smoluchowski advection–diffusion equation [10, 16, 17] or its simplified form of the asymptotic model [13, 15, 59, 60]. Some approximate methods were proposed to simulate the electroporation process with more cells or tissues without evolution of pore radius, such as a cell chain by assuming the same radius for all pores [61], and the tissues by using homogeneity method [62–64] or equivalent circuit method [65] for the calculation domain. Equivalent circuit method can be employed to reduce the large computational cost with finite element method to get the transmembrane voltage [17, 65]; however, it limits the need to obtain detailed spatial distribution of parameters under complex cell arrangements. In this work, to understand the DNA delivery mechanism during the TNT approach, both the cell-array-based delivery model and the multilayer-stack-based delivery model were employed to perform the simulation at the single cell level and tissue level, respectively.

3.2.1 Cell array-based delivery model—Figure 2(a) shows a physical model of a needle attached on the skin with 35 V applied, generating an effective electric field across the cell array similar as applying 150 V in the TNT experiment where the mouse skin thickness is about 1 mm. The nominal electric field is calculated as 150 V/mm, though the effective electric field across the tissue is ~ 126 V/mm because some voltage drops across the needle. The tissue layer is simplified as a unit domain (an 8 × 7 cell array) with the hexagonal arrangement of typical mammalian cells. As shown in the electric field distribution across the unit domain in Fig. 2(b), the field intensity is higher in the vicinity under the needle and gradually decreases toward the bottom of the tissue. The hollow needle array-based TNT gene delivery mainly depends on the mechanisms of electroporation and

electrophoresis. A transient permeabilization appears on the cell membrane when applying a voltage since the preexisting hydrophobic pores originating from thermal fluctuation can transfer to hydrophilic pores on the cell membrane through rearrangement of polar molecules in the phospholipid bilayer to minimize the pore energy (see SI A in the ESM) [10, 13]. Hydrophilic pores are usually considered to be responsible for the transportation of external molecules into cells. Figure 2(c) shows the relationship between pore radius and change in free energy during pore formation with different transmembrane voltages (V_m) when assuming the formation of only one pore on the cell membrane.

For a rigid method, the Smoluchowski advection–dilfusion equation is usually employed to describe the formation, evolution, and deduction of the electropores [10, 13]; however, it causes huge computational cost to solve the partial differential equations (PDEs) in a large scale. Here, we use the asymptotic model to describe the density of hydrophilic pores based on the ordinary differential equations (ODEs), read as [13, 59]

$$\frac{\mathrm{d}N(t,\theta)}{\mathrm{d}t} = \alpha \mathrm{e}^{(V_{\mathrm{m}(t,\theta)}/V_{\mathrm{cp}})^2}\left(1 - \frac{N(t,\theta)}{N_0 \mathrm{e}^{q(V_{\mathrm{m}(t,\theta)}/V_{\mathrm{ep}})^2}}\right) \quad (1)$$

where $N(t,\theta)$ is the pore number density at a specific time and position, α, V_{ep}, N_0, and q are constant values listed in Table S1 in the ESM. This asymptotic model assumes there are no hydrophilic pores at the initial condition, and the radius of created hydrophilic pores grow from an initial radius r_*. Also, with ignoring the negligible contribution of diffusion term in the Smoluchowski advection-diffusion equation, the asymptotic model mainly considers contribution of drift (or advection) factor for the evolution of the newly created hydrophilic pores, leading to the expression of the change rate of radii (r) of the total M pores written as [59]

$$\frac{\mathrm{d}r_j}{\mathrm{d}t} = v(r_j, V_{\mathrm{m}}, \tau_{\mathrm{eff}}), j = 1, 2, \ldots, M \quad (2)$$

where v is the drift velocity of the hydrophilic pores, which depends on the contribution from transmembrane voltage V_m and the effective surface tension τ_{eff} of the cell membrane (see SI B and SIC in the ESM).

pDNA molecules are known as highly negatively charged molecules, which can migrate under external electric field beside the diffusion effect. The electrokinetic movement of the charged species is governed by the Nernst–Planck equations as [66]

$$\frac{\partial c_\pm}{\partial t} = \nabla \cdot \left(D_\pm \nabla c_\pm \pm D_\pm \frac{z_\pm e}{k_B T} c_\pm \nabla \varphi - c_\pm \boldsymbol{u}\right) \quad (3)$$

where $D_\pm$ are the diffusivity coefficients of positive and negative species, $\boldsymbol{u}$ is the flow field, z is the valence of the specie (positive or negative) with concentration c, and e is the elementary charge. This equation is used to describe the mass transport of species by the contribution from diffusion, electric migration, and convection effects. The flow field $\boldsymbol{u}$ can be solved from the Navier–Stokes equation and continuity condition given in the

SI D in the ESM. Moreover, the pDNA molecules can be delivered into cells when the electropores created on the cell membrane exceed a critical radius (r_s = 10 nm) referring to the average nanopore size allowing the circular pDNA with large size to move through as reported in previous experiment [67]. The total amount of molecules transported across the cell membrane during the pulse can be calculated by integration of the molecule flux using the formular given in the SI E in the ESM.

3.2.2 Multilayer-stack-based delivery model—Using homogeneous model is an efficient way to estimate the result of the gene delivery process in a large dimension for the complex skin structure. The skin was modeled by a multilayer stack, including the epidermis, dermis, and hypodermis (or subcutaneous tissue), in this work. These tissue layers, which are similar to a porous media, vary in thicknesses and physical parameters depending on the tissue's location, sex, age, individual, and the animal species. The parameters for the mouse model can be found in the Table S3 in the ESM. Moreover, the delivery of molecules was considered as an electrokinetic flow in the porous media, which is described in the SI H in the ESM. The outmost layer of the stratum corneum, usually possessing a high density and a large resistivity [63, 64], significantly affects the delivery efficiency. In this work, mouse skin was exfoliated before the TNT procedure to reduce the influence of the stratum corneum layer, and this layer was not considered in the multilayer sack model.

3.3 Analysis of the electroporation dependency on position in the tissue cells

Bulk electroporation on a single cell presents a simple model to understand the electroporation-related behavior including the transmembrane voltages (TMV) distribution over the cell membrane, pore evolution, and pDNA molecule delivery into the cell (see Fig. S1 in the ESM). Compared to the bulk electroporation on a single cell, the physical model of the multicellular electroporation exhibits complex behaviors [62, 65, 68]. There are prominent interactions between neighboring cells that influences the electroporation behaviors as well as the electrophoresis process of the charged molecules. A periodic electric pulse of 150 V/mm, with a pulse duration of 10 ms and a pulse interval of 100 ms (shown in Fig. S2 in the ESM), is used in both the simulation model and experiment. Four cells from different locations, C1–C4, are selected for further analysis (see Fig. 2(b)). The electroporation results of cell C1 are shown in Figs. 2(d)–2(i), where the circular coordinate is used to describe the cell electroporation properties under an electric pulse of 150 V/mm. The transmembrane voltage distribution on the cell membrane is shown in Figs. 2(d) and 2(e) at different polar times and angles, respectively. After an electric pulse is applied, a high transmembrane voltage appears on the vicinity of polarized (90°) and depolarized (270°) poles of C1 cell due to the localized electric field caused by the hollow microchannel of the needle. A global distribution of the TMV on the cell membrane can be seen in Fig. S3(a) in the ESM. Upon an applied electric field, the transmembrane voltage at the pole (90°) increases, starting from rest voltage (V_{rest}) of −0.08 V and reaching its maximum of ~ 1.4 V at 0.7 μs, and maintains a stable voltage of ~ 0.5 V until the electric pulse is turned off (Fig. 2(e)). The existence of the V_{rest}, prior to the applied electric pulse, originates from the biological electric potential between cells and the extracellular environment [69]. Hydrophilic pores are mainly created shortly after the threshold of ~ 1 V, resulting in the

reduction of the membrane resistance, hence the transmembrane voltage decreases [10, 16, 17]. The changes of the membrane resistance can be found in Fig. S3(b) in the ESM, which presents the evolution of the cell membrane conductivity at different polar angles. More details of the global distribution of membrane conductivity are included in Fig. S3(c) in the ESM. In Fig. 2(f), the electropores appear first near the polar angle of 90° and then at the opposite pole area, due to a stronger localized electric field underneath the needle array. In Fig. 2(g), it shows different starting times for the formation of pores at different polar angles, and the pore density slightly decreases over time. Figure 3(a) shows the distribution of the formed pore density $N(t, \theta)$ mainly near the two poles, where there is a higher pore density near the polar angle of 90° Figure 2(h) depicts the pore evolution over time, where pores at the polar angles of 90°, 180% and 270° shrink to a local minimum radius of $r \approx 1\ nm$, while the rest stabilizes at the local minimum radii with larger values. All pores shrink quickly to a radius of ~ 1 nm in several microseconds after the applied voltage is turned off. It was reported that the resealing of the electroporated nanopores could take seconds to minutes [70], however, molecular dynamics (MD) simulation [71] revealed that the pore size drops instantly as TMV drops. The pore evolution over whole polar angles can be seen in Fig. 3(b), which shows that the pores over 20 nm are mainly located around the polarized angle (90°). As a result of the pore evolution, it leads to the corresponding changes of the ratio (ρ_p) between the local pore area and the membrane area. The representative pore area ratio distributions at different polar angles are given in Fig. 3(c). It is worth noting that the pore density plot considers all the created pores, while pore area ratio only calculates pores larger than 10 nm.

In comparison with the C1 cell, electroporation behaviors of the C2–C4 cells exhibit different characteristics. As seen in the Fig. 3(d), for the C2 cell, the TMV distributes in an asymmetric way, with the polarized pole at ~30° and the depolarized pole around ~212°. The C2 cell possesses a relatively higher pore density in the vicinity of the depolarized pole rather than the polarized position as observed for the C1 cell; however, the maximum pore density on the C2 cell membrane is much smaller compared to the C1 cell, owing to the localized electric field. In Fig. 3(f), the distribution of the ratio of pore area (ρ_p) matches the distribution of the pore density, and shows a lower ratio value referring to that of the C1 cell. This ratio distribution is supported by the pore radius distribution shown in Fig. 3(e). Moreover, similar electroporation behavior is found for the C3 and C4 cells (Figs. 3(g)–3(i) and 3(k)–3(m), respectively), which have the asymmetric distribution of the transmembrane voltage with different polarized poles because of the nonuniform electric field. The pores were generated subsequently from C1 to C4 over time as seen in Fig. 3(c), because the resistance of the electroporated cells dynamically changes during a pulse duration, resulting in a redistribution of the electric field across the cells. The preexisting pores from previous pulses contribute to the resistance reduction, which causes different initial conditions for the next pulse. Figure 3(n) illustrates the comparison of TMV distributions on the cell membrane of the cells C1–C4 reaching their maximum TMV values at 0.7, 1.6, 2.9, and 6.4 μs, respectively. It shows the changes of the polarized pole positions of each cell and a gradual decrease in the maximum TMV value from C1 to C4, due to the reduced electric field strengths at their specific locations within the skin (Fig. 2(b)). As seen in Figs. 3(o) and 3(p), many pores are created on cell C1, whilst the pores with radius larger than the critical

radius only take up a small ratio compared to the other cells. This is consistent with previous reports that higher voltage induces large number of small pores, while lower voltage creates more large pores [17, 72, 73].

3.4 Analysis of electroporation dependency on the electric field strength in tissue

Electric field strength is the critical parameter for determining the pore formation and evolution during the electroporation. Especially, it can arise the safety concern for cell viability if the electric field strength is over a certain value. To find an optimal electric field for maximizing the transfection efficiency, we investigated the effect of the electroporation parameters by changing the amplitude of the electric pulses, ranging from 50 to 200 V/mm with an interval of 50 V/mm. The nominal electric field strength of 50, 100, and 200 V/mm corresponds to an effective electric field strength of 46, 92, and 153 V/mm on the skin, respectively, considering the voltage drop across the needle.

A typical internal cell within the skin structure, C3, was chosen to investigate the electroporation behavior of skin cells subject to electric pulses with different electric field strengths as seen in Fig. 4. The case of 150 V/mm has been discussed previously in Fig. 3. The maximum TMV value increases as the electric field strength of the electric pulse increases as seen in Figs. 4(a), 4(e), and 4(i). For instance, as the electric pulse amplitude increases, the maximum V_m at polar angle of 90° increases from ~ 0.4 to 1.2 V, and the time to reach their maximum V_m is reduced from ~11 to ~2 μs, implying that a shortened time is needed for electropore formation as the electric field increases. Under an electric pulse of 50 V/mm, since the maximum V_m is ~ 0.4 V, it is too low to create electropores on the C3 cell (Fig. 4(c)), which results in zero pore area ratio (Fig. 4(d)). Electropores are generated on the C3 cell when the electric field is over 100 V/mm with the maximum pore size being ~ 25 nm (Fig. 4(g) and 4(k)). Similarly, we performed the same calculations on the C1 cell to compare the electroporation behaviors with the C3 cell as seen in Fig. S4 in the ESM. The main difference is that the C1 cell creates electropores at 50 V/mm, due to the stronger localized electric field as seen in Figs. S4(c) and S4(d) in the ESM. Moreover, the pores are generated on the C1 cell more quickly compared with the C3 cell, as the time to reach the maximum V_m is shorter.

Figure 5 shows the pore evolution in a half plane across the skin structure at different electric pulses. We assumed that the pDNA used in this work can translocate into cells via the electropores with their radii over the critical radius, hence we plotted only the results of larger pore ($r > r_s$) in Fig. 5. Under a lower electric pulse of 50 V/mm, only the C1 cell forms electropores ($r > r_s$), thanks to the strong electric field that is only localized underneath the needle, implying that larger molecules can only translocate into cells located within a shallow layer of skin. At 100 V/mm, the pores ($r > r_s$) are generated first on the C1 cell, then gradually spread into the deeper tissue, finally reaching 25% of electroporated cells after the 3rd pulse. Interestingly, the number of electroporated cells ($r > r_s$) was slightly reduced in the 3rd pulse compared to the 2nd pulse, because each pulse results in different initial conditions for the next pulse, hence the electroporation result for each pulse is not identical. When the voltage increased to 150 V/mm, the electropores ($r > r_s$) gradually spread from the C1 cell across the whole tissue laterally and vertically, and 82% of the cells

were electroporated in the unit domain after the 3rd pulse. If the voltage increased further to 200 V/mm, 83% of the cells were electroporated through the skin structure, which is similar to the result of 150 V/mm. In conclusion, the percentage of electroporated cells ($r > r_s$) can reach 82%–83% at electric fields, ranging from 150 to 200 V/mm.

3.5 Molecules transport in the tissue cells

The mechanism of the gene uptake process during the electroporation is complex and not fully understood yet [12]. Smaller sizes of genes less than 15 bp can freely enter into cells through electroporated nanopores [74], while larger sizes of genes form a membrane–gene complex and translocate into cells via either a combined steps of insertion and translocation across the membrane in several seconds [75, 76] or an endocytosis-like process which takes minutes to complete the internalization [77]. Meanwhile, large DNA molecules with sizes ranging from 25 to 20,000 bp can freely translocate into giant unilamellar vesicles (GUVs) with electrophoretic force [78]. It was reported that, a pDNA with a size of 9,500 bp and a hydrodynamic diameter of 380 nm can penetrate through nanopores with size ranging from 10 to 30 nm under a propriate pressure by stretching into long hair-shaped flexible strands [67]. In this work, the pDNA used in the simulation has a size ranging from 4,000 to 12,000 bp. Especially, the simulation of electroporation and electrophoresis was mainly performed on a typical large molecule with a size of 5,494 bp and a hydrodynamic radius of ~ 200 nm. To calculate the DNA flux and concentration profile across the skin, we assumed that the pDNA can freely translocate into and out of cells via electropores ($r > rs$) without considering other biological transport such as endocytosis and fusion. In fact, the gene translocation mechanism is sophisticated, where parameters such as the cell size and type, membrane composition involving proteins and cholesterol, cytoskeleton network supporting the membrane, extracellular environment, and electric pulse parameters affect the uptake process [12, 20, 67, 74]. Thus, a direct observation technique with nanoseconds imaging and nanoscale resolution is required to further investigate the uptake mechanism in the future.

The transport behavior of the pDNA subject to the electric pulse of 150 V/mm is presented in Fig. 6. The flow flux across the membrane of the C2 cell at the polarized pole (~40°) is plotted in Fig. 6(a). Figure 6(b) calculates the flow flux of the pDNA at 119 and 229 ms. The distribution of the flow flux follows the pattern of the local pore area ratio. In Fig. 6(c), almost no molecules are being delivered into the C2 cell during pulse 1 because the flow flux is close to zero as seen in Fig. 6(a). A certain number of molecules can be accumulated within the cell with more pulse numbers as seen in Fig. 6(c). With the assistance of electric pulses, the pDNA molecules can be delivered into the tissue cells via electroporated pores ($r > r_s$) by the electrophoretic force. Figure S5(a) in the ESM gives the flow velocity field of the pDNA, while Figs. S5(b)–S5(e) in the ESM plot the streamline profile in the unit domain at the third electric pulse, from where it clearly shows the DNA transport paths. Under the electric pulse of 150 V/mm, the delivery depth increases gradually as the number of pulses increases, reaching a depth of ~ 110 μm through extracellular space after pulse 3 as shown in Fig. 6(g). The influence of different voltages on the transport behavior is compared in Figs. 6(h)–6(j), where higher voltage delivers deeper and wider compared to lower voltages.

3.6 Comparison between the simulation and experiment for *in vivo* TNT

To compare between the simulation and experiment results, a larger calculation domain was needed for a tissue thickness of ~ 1 mm to be comparable with the TNT procedure used on the mouse skin. This work adopted the multilayer-stack-based model to simulate the DNA delivery process in the skin. Figure 7(a) presents the simulation result based on pDNA of *Ascl1*, which shows the relationship between the delivery depth and the number of pulses under an electric pulse of 200 V (nominally 200 V/mm), reaching a maximum delivery depth of ~ 550 μm after 10 pulses. Figure 7(b) shows the calculation results of the molecules transport in a skin after 10 pulses at 50, 100, 150, and 200 V, respectively. A gradual increase in the delivery depth was found when the applied voltage increases. As shown in Figs. 7(c)–7(e), to validate the gene delivery simulation, *Ascl1* expressing plasmid was delivered on exfoliated mouse skin (C57BF/6 mice, aged 18 weeks) using TNT at 100 and 200 V, respectively. The tissue was collected in OCT for cryosectioning 24 h post TNT procedure. Tissues from epidermis and dermis were captured separately using laser captured microdissection for quantitative analysis of *Ascl1* expression. As shown in Figs. 7(f) and 7(g), gene delivery at the electric pulse of 100 V shows significant expression in the epidermis while 200 V shows significant expression in the dermis, indicating that the pDNA was delivered to a deeper region and achieved successful expression within more cells at the deeper region as the electric pulse voltage increases. Thus, by controlling the voltage of applied electric pulse, it allows us to control the gene delivery and expression at a certain region for specific therapeutic purposes.

In addition, the influence of the pDNA selection is mainly examined through their molecule size, which can affect the effective charge of the DNA molecule and consequently the delivery process. As shown in the Fig. S6(a) in the ESM, a variety of plasmid DNA sizes were investigated in the simulation with the multilayer-stack based model. By assuming a constant effective charge that is reasonable for charged molecules in the saturated scenario [79], the simulation shows a decreasing trend for the delivery depth as the DNA size increase. However, the simulation results of the delivery depth can be overestimated for large size and underestimated for small size. This is because other factors, such as the DNA size-dependent diffusion coefficients in the complex skin structure, are not fully considered in the simulation, which may lead to the stronger or saturable resistance for the delivery of DNA with very larger size and the reversed scenario for smaller size. More details of the effective charge of pDNA can be found in the SI F in the ESM. Moreover, the delivery depth is significantly affected by an existing stratum corneum layer as shown in the Fig. S7 in the ESM, hence exfoliating the layer prior to the TNT procedure is critical to achieve a high transfection efficiency. Furthermore, the research results in this work were obtained from the mouse-based skin model, which is different from the human skin model because of the differences in the skin structures and biophysical characteristics [80, 81]. For instance, the dermal layer of humans is usually much thicker than that of the mouse, resulting in the distinguished delivery behaviors [45]. Thus, improved numerical models and precise experimental validation are needed in future investigations.

Lastly, this work is conducted for mainly three purposes, to explain the underlying mechanism, find the optimal voltage parameter of the gene delivery process in the TNT

method through the combination of simulation and experiment, as well as to pave the path for expanding the applications of *in vivo* TNT method from the mouse model to pig model, and eventually to human model. Generally, if without simulation, one may experience difficulties in implementing the *in vivo* TNT to a new animal or human model in a safe, efficient, predictive, and low-cost way. This is because the multilayered skin structure can vary in geometric parameters (such as thickness variations) and electrical properties (such as the effective conductivity) for different models [45–47, 63], affecting the gene delivery and expression results.

3.7 Future applications of the *in vivo* TNT

The TNT method presents an efficient and well-controlled *in vivo* transfection approach that directly translocate exogeneous genes to target tissues using electric pulses, showing a variety of promising therapeutic applications in the future, which mainly includes specific cell reprogramming, drug or DNA vacancy delivery, and intracellular biological molecules sampling. The induced neurons were proved to be useful in improving the stroke-affected site of mouse brains, while induced endothelial cells were found to successfully rescue tissue necrosis by forming functional blood vessels [1]. Moreover, to avoid the drug or vaccine specific immune responses and improve the delivery efficiency [22–24], TNT method can also be employed for intradermal delivery of electrically charged drug or vacancies in one, efficient step, rather than the conventional two-steps delivery with electroporation and subsequent injection [24]. Additionally, compared with the sampling function realized by nanostraw based electroporation platform [82], hollow needle-array-based TNT method provides an alternative way of sampling intracellular biomolecules or specific biomarkers in the deep tissue layer in order to investigate or continuously monitor the biological activities of tissue cells for therapeutic diagnosis. Eventually, after completing the investigation of the functioning mechanisms and safety concern on animal and human models, the *in vivo* TNT will be used to develop various new therapeutic applications in the fields of regenerative medicine, drug delivery, and advanced diagnosis for humans in the future.

4 Conclusions

This work addresses the gene delivery process during the *in vivo* tissue nanotransfection. In the cell-array-based delivery model, the asymptotic method for electroporation was employed to simulate electroporation behaviors of the tissue cells located at different positions. The analysis of the position-dependent electroporation on the tissue cells shows prominent variations of the pore formation locations on the membrane, and a large reduction of the local pore density and area ratio, resulting from the nonuniform electric field distribution as well as the interaction between cells. Hence, electroporated cells obtain different amount of transported pDNA molecules based on their locations within the tissue. Also, the analysis of the electric field strength-dependency indicates that a larger voltage causes an increase in delivery area and depth. The percentage of electroporated cells with a pore radius over 10 nm increases as the applied voltage increases. The percentage was 25% for 100 V/mm, but significantly increased to 82% at 150 V/mm, indicating that a moderate electric field strength, such as 150 V/mm, is expected to be a balance between the delivery

efficiency and safety concerns. Moreover, multilayer-stack-based model analysis found that the delivery depth increases rapidly after breaking through the densely packed epidermis layer. It is important to mention that the stratum corneum layer significantly blocks the gene delivery owing to its high density and low conductivity, thus mouse skin is required to be exfoliated before the TNT operation. In the *in vivo* TNT experiment conducted on the mouse skin, the obtained delivery depths of pDNA matches well with the simulation results using the model. Successful gene expression was also observed in the target tissue cells. The combination of simulation and experiment in this work provides a better understanding of the underlying mechanisms for *in vivo* TNT approach, offering guidance and insight for future clinical applications for humans.

Supplementary Material

Refer to Web version on PubMed Central for supplementary material.

Acknowledgements

This work was supported in part by National Institutes of Health (NIH) grant (No. DK128845) and Department of Defense grant (Nos. W81XWH-21-1-0097, W81XWH-21-1-0033, and W81XWH-20-1-251) to C.K.S, NIH grant (No. GM143572) to Y.X, and NIH grant (No. DK129592) to S.G.

References

[1]. Gallego-Perez D; Pal D; Ghatak S; Malkoc V; Higuita-Castro N; Gnyawali S; Chang LQ; Liao WC; Shi JF; Sinha M et al. Topical tissue nano-transfection mediates non-viral stroma reprogramming and rescue. Nat. Nanotechnol 2017, 12, 974–979. [PubMed: 28785092]

[2]. Zhou XJ; Brown BA; Siegel AP; El Masry MS; Zeng XY; Song WR; Das A; Khandelwal P; Clark A; Singh K et al. Exosome-mediated crosstalk between keratinocytes and macrophages in cutaneous wound healing. ACS Nano 2020, 14, 12732–12748. [PubMed: 32931251]

[3]. Lemmerman LR; Balch MHH; Moore JT; Alzate-Correa D; Rincon-Benavides MA; Salazar-Puerta A; Gnyawali S; Hairis HN; Lawrence W; Ortega-Pineda L et al. Nanotransfection-based vasculogenic cell reprogramming drives functional recovery in a mouse model of ischemic stroke. Sci. Adv 2021, 7, eabd4735. [PubMed: 33741587]

[4]. Xuan Y; Ghatak S; Clark A; Li Z; Khanna S; Pak D; Agarwal M; Roy S; Duda P; Sen CK Fabrication and use of silicon hollow needle arrays to achieve tissue nanotransfection in mouse tissue *in vivo*. Nat. Protoc, 2021, 16: 5707–5738. [PubMed: 34837085]

[5]. Takahashi K; Yamanaka S Induction of pluripotent stem cells from mouse embryonic and adult fibroblast cultures by defined factors. Cell 2006, 126, 663–676. [PubMed: 16904174]

[6]. Mao AS; Mooney DJ Regenerative medicine: Current therapies and future directions. Proc. Natl. Acad. Sci. USA 2015, 112, 14452–14459. [PubMed: 26598661]

[7]. Srivastava D; DeWitt N *In vivo* cellular reprogramming: The next generation. Cell 2016, 166, 1386–1396. [PubMed: 27610565]

[8]. Mount NM; Ward SJ; Kefalas P; Hyllner J Cell-based therapy technology classifications and translational challenges. Philos. Trans. R. Soc. Lond. B Biol. Sci 2015, 370, 20150017. [PubMed: 26416686]

[9]. Hardee CL; Arévalo-Soliz LM; Homstein BD; Zechiedrich L Advances in non-viral DNA vectors for gene therapy. Genes 2017, 5, 65.

[10]. Weaver JC; Chizmadzhev YA Theory of electroporation: A review. Bioelectrochem. Bioenerg 1996, 41, 135–160.

[11]. Shi JF; Ma YF; Zhu J; Chen YX; Sun YT; Yao YC; Yang ZG; Xie J A review on electroporation-based intracellular delivery. Molecules 2018, 23, 3044.

[12]. Kotnik T; Rems L; Tarek M; Miklavčič D Membrane electroporation and electropermeabilization:Mechanisms and models. Annu. Rev. Biophys 2019, 48, 63–91. [PubMed: 30786231]

[13]. Neu JC; Krassowska W Asymptotic model of electroporation. Phys. Rev. E 1999, 59, 3471–3482.

[14]. Tryfona T; Bustard MT Enhancement of biomolecule transport by electroporation: A review of theory and practical application to transformation of *Corynebacterium glutamicum*. Biotechnol. Bioeng 2006, 93, 413–423. [PubMed: 16224791]

[15]. Li JB; Lin H Numerical simulation of molecular uptake via electroporation. Bioelectrochemistry 2011, 82, 10–21. [PubMed: 21621484]

[16]. Son RS; Gowrishankar TR; Smith KC; Weaver JC Modeling a conventional electroporation pulse train: Decreased pore number, cumulative calcium transport and an example of electrosensitization. IEEE Trans. Biomed. Eng 2016, 63, 571–580. [PubMed: 26302502]

[17]. Mukherjee P; Nathamgari SSP; Kessler JA; Espinosa HD Combined numerical and experimental investigation of localized electroporation-based cell transfection and sampling. ACS Nano 2017, 12, 12118–12128.

[18]. Cao YH; Ma EB; Cestellos-Blanco S; Zhang B; Qiu RY; Su YD; Doudna JA; Yang PD Nontoxic nanopore electroporation for effective intracellular delivery of biological macromolecules. Proc. Natl. Acad. Sci. USA 2019, 116, 7899–7904. [PubMed: 30923112]

[19]. Perrier DL; Vahid A; Kathavi V; Stam L; Rems L; Mulla Y; Muralidharan A; Koenderink GH; Kreutzer MT; Boukany PE Response of an actin network in vesicles under electric pulses. Sci. Rep 2019, 9, 8151. [PubMed: 31148577]

[20]. André F; Mir LM DNA electrotransfer: Its principles and an updated review of its therapeutic applications. Gene Ther. 2004, 11, S33–S42. [PubMed: 15454955]

[21]. Gehl J; Sersa G; Matthiessen LW; Muir T; Soden D; Occhini A; Quaglino P; Curatolo P; Campana LG; Kunte C et al. Updated standard operating procedures for electrochemotherapy of cutaneous tumours and skin metastases. Acta Oncol. 2018, 57, 874–882. [PubMed: 29577784]

[22]. Kim K; Lee WG Electroporation for nanomedicine: A review. J. Mater. Chem. B 2017, 5, 2726–2738. [PubMed: 32264158]

[23]. Luckay A; Sidhu MK; Kjeken R; Megati S; Chong SY; Roopchand V; Garcia-Hand D; Abdullah R; Braun R; Montefiori DC et al. Effect of plasmid DNA vaccine design and *in vivo* electroporation on the resulting vaccine-specific immune responses in rhesus macaques. J. Virol 2007, 81, 5257–5269. [PubMed: 17329330]

[24]. Todorova B; Adam L; Culina S; Boisgard R; Martinon F; Cosma A; Ustav M; Kortulewski T; Le Grand R; Chapon C Electroporation as a vaccine delivery system and a natural adjuvant to intradermal administration of plasmid DNA in macaques. Sci. Rep 2017, 7, 4122. [PubMed: 28646234]

[25]. Xie X; Xu AM; Leal-Ortiz S; Cao YH; Gamer CC; Melosh NA Nanostraw-electroporation system for highly efficient intracellular delivery and transfection. ACS Nano 2013, 7, 4351–4358. [PubMed: 23597131]

[26]. Cao Y; Chen H; Qiu R; Hanna M; Ma E; Hjort M; Zhang A; Lewis RS; Wu JC; Melosh NA Universal intracellular biomolecule delivery with precise dosage control. Sci. Adv 2018, 4, eaat8131. [PubMed: 30402539]

[27]. Wen R; Zhang AH; Liu D; Feng JM; Yang J; Xia DH; Wang J; Li CW; Zhang T; Hu N et al. Intracellular delivery and sensing system based on electroplated conductive nanostraw arrays. ACS Appl. Mater. Interfaces 2019, 11, 43936–43948. [PubMed: 31696695]

[28]. Mahnič-Kalamiza S; Vorobiev E; Miklavčič D Electroporation in food processing and biorefinery. J. Membr. Biol 2014, 247, 1279–1304. [PubMed: 25287023]

[29]. Asträin-Red[ISP]in L; Raso J; Cebrián G; [ISP]Alvarez I Potential of pulsed electric fields for the preparation of Spanish dry-cured sausages. Sci. Rep 2019, 9, 16042. [PubMed: 31690768]

[30]. Huo ZY; Luo YF; Xie X; Feng C; Jiang KL; Wang JP; Hu HY Carbon-nanotube sponges enabling highly efficient and reliable cell inactivation by low-voltage electroporation. Environ. Sci. Nano 2017, 4, 2010–2017.

[31]. Wang Y; Yang Y; Yan L; Kwok SY; Li W; Wang ZG; Zhu XY; Zhu GY; Zhang WJ; Chen XF et al. Poking cells for efficient vector-free intracellular delivery. Nat. Commun 2014, 5, 4466. [PubMed: 25072981]

[32]. Sharei A; Zoldan J; Adamo A; Sim WY; Cho N; Jackson E; Mao S; Schneider S; Han MJ; Lytton-Jean A et al. A vector-free microfluidic platform for intracellular delivery. Proc. Natl. Acad. Sci. USA 2013, 110, 2082–2087. [PubMed: 23341631]

[33]. Urban P; Kirchner SR; Mühlbauer C; Lohmuller T; Feldmann J Reversible control of current across lipid membranes by local heating. Sci. Rep 2016, 6, 22686. [PubMed: 26940847]

[34]. Kay MA; Glorioso JC; Naldini L Viral vectors for gene therapy: The art of turning infectious agents into vehicles of therapeutics. Nat. Med 2001, 7, 33–40. [PubMed: 11135613]

[35]. Wang QY; Yu JJ; Kadungure T; Beyene J; Zhang H; Lu Q ARMMs as a versatile platform for intracellular delivery of macromolecules. Nat. Commun 2018, 9, 960. [PubMed: 29511190]

[36]. Kurosawa O; Oana H; Matsuoka S; Noma A; Kotera H; Washizu M Electroporation through a micro-fabricated orifice and its application to the measurement of cell response to external stimuli. Meas. Sci. Technol 2006, 17, 3127–3133.

[37]. Fei ZZ; Hu X; Choi HW; Wang SN; Farson D; Lee LJ Micronozzle array enhanced sandwich electroporation of embryonic stem cells. Anal. Chem 2010, 52, 353–358.

[38]. Adamo A; Arione A; Sharei A; Jensen KF Flow-through comb electroporation device for delivery of macromolecules. Anal. Chem 2013, 55, 1637–1641.

[39]. Dong ZZ; Jiao YL; Xie BT; Hao YC; Wang P; Liu YY; Shi JF; Chitrakar C; Black S; Wang YC et al. On-chip multiplexed single-cell patterning and controllable intracellular delivery. Microsyst. Nanoeng 2020, 6, 2. [PubMed: 34567617]

[40]. Rojas-Chapana JA; Correa-Duarte MA; Ren ZF; Kempa K; Giersig M Enhanced introduction of gold nanoparticles into vital *Acidothiobacillus ferrooxidans* by carbon nanotube-based microwave electroporation. Nano Lett. 2004, 4, 985–988.

[41]. Xie C; Lin ZL; Hanson L; Cui Y; Cui BX Intracellular recording of action potentials by nanopillar electroporation. Nat. Nanotechnol 2012, 7, 185–190. [PubMed: 22327876]

[42]. Boukany PE; Morss A; Liao WC; Henslee B; Jung H; Zhang XL; Yu B; Wang XM; Wu Y; Li L et al. Nanochannel electroporation delivers precise amounts of biomolecules into living cells. Nat. Nanotechnol 2011, 6, 747–754. [PubMed: 22002097]

[43]. Petchsangsai M; Rojanarata T; Opanasopit P; Ngawhirunpat T The combination of microneedles with electroporation and sonophoresis to enhance hydrophilic macromolecule skin penetration. Biol. Pharm. Bull 2014, 37, 1373–1382. [PubMed: 24931312]

[44]. Huang D; Zhao DY; Wang XX; Li CH; Yang TR; Du LL; Wei ZW; Cheng Q; Cao HQ; Liang ZC et al. Efficient delivery of nucleic acid molecules into skin by combined use of microneedle roller and flexible interdigitated electroporation array. Theranostics 2018, 8, 2361–2376. [PubMed: 29721085]

[45]. Wei JCJ; Edwards GA; Martin DJ; Huang H; Crichton ML; Kendall MAF Allometric scaling of skin thickness, elasticity, viscoelasticity to mass for micro-medical device translation: From mice, rats, rabbits, pigs to humans. Sci. Rep 2017, 7, 15885. [PubMed: 29162871]

[46]. Bahri OA; Naldaiz-Gastesi N; Kennedy DC; Wheatley AM; Izeta A; McCullagh KJA The *panniculus carnosus* muscle: A novel model of striated muscle regeneration that exhibits sex differences in the *mdx* mouse. Sci. Rep 2019, 9, 15964. [PubMed: 31685850]

[47]. Kopcewicz M; Walendzik K; Bukowska J; Kur-Piotrowska A; Machcinska S; Gimble JM; Gawronska-Kozak B Cutaneous wound healing in aged, high fat diet-induced obese female or male C57BL/6 mice. Aging 2020, 12, 7066–7111. [PubMed: 32294622]

[48]. Zhang L; Li LN; .An ZL; Hoffman RM; Hofmann GA *In vivo* transdermal delivery of large molecules by pressure-mediated electroincorporation and electroporation: A novel method for drug and gene delivery. Bioelectrochem. Bioenerg 1997, 42, 283–292.

[49]. COMSOL Multiphysics®. COMSOL Multiphysics Modcling Guide. COMSOL: Stockholm, 2008.

[50]. Zuo YH; Lu SL Dermis, acellular dermal matrix, and fibroblasts from different layers of pig skin exhibit different profibrotic characteristics: Evidence from *In vivo* study. Oncotarget 2017, 5, 23613–23627.

[51]. Roy S; Sen CK; Ghatak S; Higuita-Castro N; Palakurti R; Nalluri N; Clark A; Stewart R; Gallego-Perez D; Prater DN et al. Neurogenic tissue nanotransfection in the management of cutaneous diabetic polyneuropathy. Nanomed. Nanotechnol. Biol. Med 2020, 28, 102220.

[52]. Ahmed NS; Ghatak S; El Masry MS; Gnyawali SC; Roy S; Arner M; Everts H; Sen CK; Khanna S Epidermal E-cadherin dependent β-catenin pathway is phytochemical inducible and accelerates anagen hair cycling. Mol. Ther 2017, 25, 2502–2512. [PubMed: 28803863]

[53]. Kuhn DE; Roy S; Radtke J; Khanna S; Sen CK Laser microdissection and capture of pure cardiomyocytes and fibroblasts from infarcted heart regions: Perceived hyperoxia induces p21 in peri-infarct myocytes. Am. J. Physiol. Heart Circ. Physiol 2007, 292, H1245–H1253. [PubMed: 17158647]

[54]. Ghatak S; Li JL; Chan YC; Gnyawali SC; Steen E; Yung AC; Khanna S; Roy S; Lee RJ; Sen CK AntihypoxamiR functionalized gramicidin lipid nanoparticles rescue against ischemic memory improving cutaneous wound healing. Nanomed. Nanotechnol. Biol. Med 2016, 12, 1827–1831.

[55]. Gardeniers HJGE; Luttge R; Berenschot EJW; De Boer MJ; Yeshurun SY; Hefetz M; Van't Oever R; Van Den Berg A Silicon micromachined hollow microneedles for transdermal liquid transport. J. Microelectromech. Syst 2003, 12, 855–862.

[56]. Wilke N; Mulcahy A; Ye SR; Morrissey A Process optimization and characterization of silicon microneedles fabricated by wet etch technology. Microelectron. J 2005, 36, 650–656.

[57]. Li Y; Zhang H; Yang RF; Laffitte Y; Schmill U; Hu WH; Kaddoura M; Blondeel EJM; Cui B Fabrication of sharp silicon hollow microneedles by deep-reactive ion etching towards minimally invasive diagnostics. Microsyst. Nanoeng 2019, 5, 41. [PubMed: 31636931]

[58]. Kang SK; Murphy RKJ; Hwang SW; Lee SM; Harburg DV; Krueger NA; Shin J; Gamble P; Cheng HY; Yu S et al. Bioresorbable silicon electronic sensors for the brain. Nature 2016, 530, 71–76. [PubMed: 26779949]

[59]. Krassowska W; Filev PD Modeling electroporation in a single cell. Biophys. J 2007, 92, 404–417. [PubMed: 17056739]

[60]. Moran JL; Dingari NN; Garcia PA; Buie CR Numerical study of the effect of soft layer properties on bacterial electroporation. Bioelectrochemistry 2018, 123, 261–272. [PubMed: 29146422]

[61]. Rems L; U[ISP]saj M; Kandu[ISP]ser M; Rebersek M; Miklavčič D; Pucihar G Cell electrofusion using nanosecond electric pulses. Sci. Rep 2013, 5, 3382.

[62]. Dermol-[ISP]Ceme J Miklavčič D From cell to tissue properties-modeling skin electroporation with pore and local transport region formation. IEEE Trans. Biomed. Eng 2018, 65, 458–468. [PubMed: 29364121]

[63]. Pav[ISP]selj N; Préat V; Miklavčič D A numerical model of skin electropermeabilization based on *In vivo* experiments. Ann. Biomed. Eng 2007, 35, 2138–2144. [PubMed: 17849185]

[64]. Forjanič T; Miklavčič D Numerical study of gene electrotransfer efficiency based on electroporation volume and electrophoretic movement of plasmid DNA. BioMed. Eng. OnLine 2018, 17, 80. [PubMed: 29914508]

[65]. Chizmadzhev YA; Indenbom AV; Kuzmin PL; Galichenko SV; Weaver JC; Potts RO Electrical properties of skin at moderate voltages: Contribution of appendageal macropores. Biophys. J 1998, 74, 843–856. [PubMed: 9533696]

[66]. Qiu BL; Gong LY; Li ZR; Han J Electrokinetic flow in the U-shaped micro-nanochannels. Theor. Appl. Mech. Lett 2019, 9, 36–42.

[67]. Arkhangelsky E; Sefi Y; Hajaj B; Rothenberg G; Gitis V Kinetics and mechanism of plasmid DNA penetration through nanopores. J. Membr. Sci 2011, 371, 45–51.

[68]. Gowrishankar TR; Stewart C; Weaver JC Electroporation of a multicellular system: Asymptotic model analysis. In The 26th Annual International Conference of the IEEE Engineering in Medicine and Biology Society, San Francisco, 2004, pp 5444–5446.

[69]. Wright SH Generation of resting membrane potential. Adv. Physiol. Educ 2004, 25, 139–142.

[70]. Yarmush ML; Golberg A; Ser[ISP]sa G; Kotnik T; Miklavčič D Electroporation-based technologies for medicine: Principles, applications, and challenges. Annu. Rev. Biomed. Eng 2014, 16, 295–320. [PubMed: 24905876]

[71]. Delemotte L; Tarek M Molecular dynamics simulations of lipid membrane electroporation. J. Membr. Biol 2012, 245, 531–543. [PubMed: 22644388]

[72]. Vasilkoski Z; Esser AT; Gowrishankar TR; Weaver JC Membrane electroporation: The absolute rate equation and nanosecond time scale pore creation. Phys. Rev. E 2006, 74, 021904.

[73]. Chang LQ; Li L; Shi JF; Sheng Y; Lu W; Gallego-Perez D; Lee LJ Micro-/nanoscale electroporation. Lab Chip 2016, 16, 4047–4062. [PubMed: 27713986]

[74]. Sachdev S; Moreira SF; Keehnen Y; Rems L; Kreutzer MT; Boukany PE DNA-membrane complex formation during electroporation is DNA size-dependent. Biochim. Biophys. Acta Biomembr 2020, 1862, 183089. [PubMed: 31678021]

[75]. Klenchin VA; Sukharev SI; Serov SM; Chemomordik LV; Chizmadzhev YA Electrically induced DNA uptake by cells is a fast process involving DNA electrophoresis. Biophys. J 1991, 60, 804–811. [PubMed: 1660315]

[76]. Pavlin M; Flisar K; Kanduser M The role of electrophoresis in gene electrotransfer. J. Membr. Biol 2010, 236, 75–79. [PubMed: 20640850]

[77]. Wang LL; Miller SE; Yuan F Ultrastructural analysis of vesicular transport in electrotransfection. Microsc. Microanal 2018, 24, 553–563. [PubMed: 30334512]

[78]. Sachdev S; Muralidharan A; Choudhary DK; Perrier DL; Rems L; Kreutzer MT; Boukany PE DNA translocation to giant unilamellar vesicles during electroporation is independent of DNA size. Soft Matter 2019, 15, 9187–9194. [PubMed: 31595286]

[79]. Wong PK; Wang TH; Deval JH; Ho CM Electrokinetics in micro devices for biotechnology applications. IEEE/ASME Trans. Mechatron 2004, 9, 366–376.

[80]. Gerber PA; Buhren BA; Schrumpf H; Homey B; Zlotnik A; Hevezi P The top skin-associated genes: A comparative analysis of human and mouse skin transcriptomes. Biol. Chem 2014, 395, 577–591. [PubMed: 24497224]

[81]. Zomer HD; Trentin AG Skin wound healing in humans and mice: Challenges in translational research. J. Dermatol. Sci 2018, 90, 3–12. [PubMed: 29289417]

[82]. Cao YH; Hjort M; Chen HD; Birey F; Leal-Ortiz SA; Han AM; Santiago JG; Pasca SP; Wu JC; Melosh NA Nondestructive nanostraw intracellular sampling for longitudinal cell monitoring. Proc. Natl. Acad. Sci. USA 2017, 114, E1866–E1874. [PubMed: 28223521]

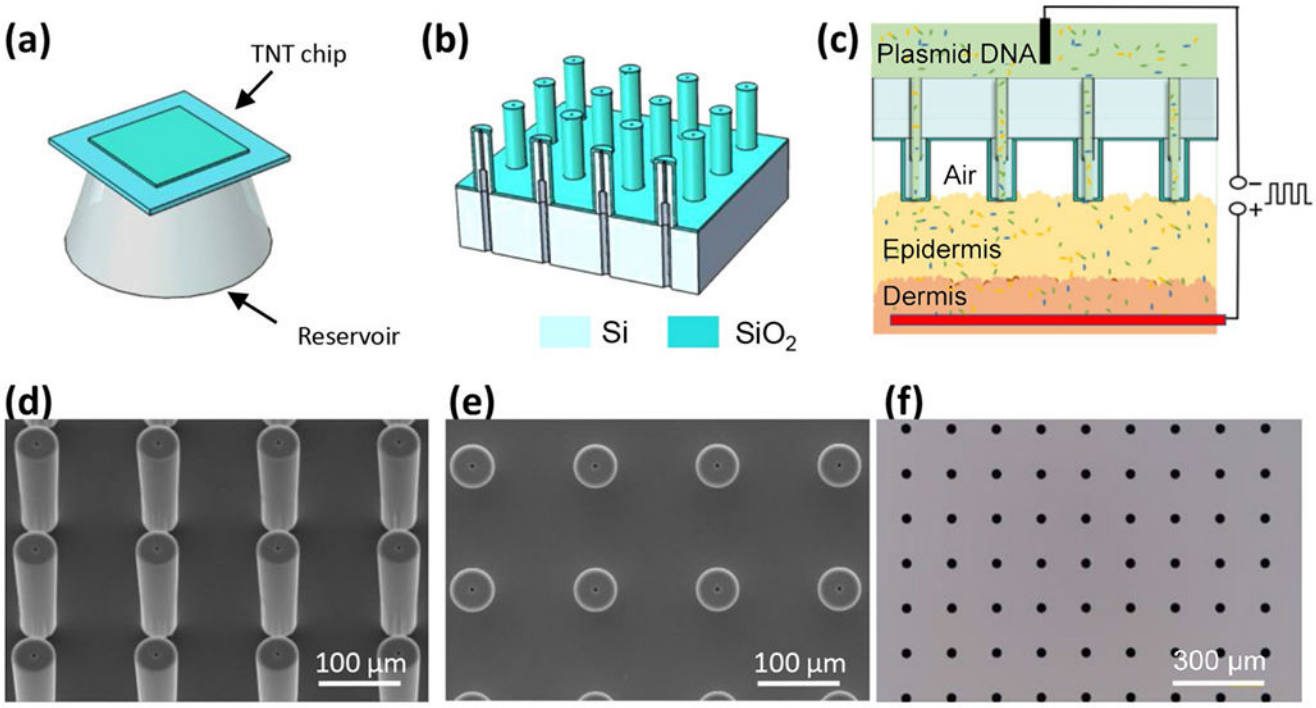

Figure 1.

Hollow needle-based TNT approach. (a) A TNT chip attached onto the reservoir. (b) A schematic design showing Si hollow needle array with flat tip. (c) A schematic of delivering plasmid DNA to skin tissue with hollow needle array and electric pules. SEM images of the fabricated silicon hollow needle array in (d) tilted view and (e) top view, respectively. (f) An optical image of hollow microchannel array on the backside of the chip.

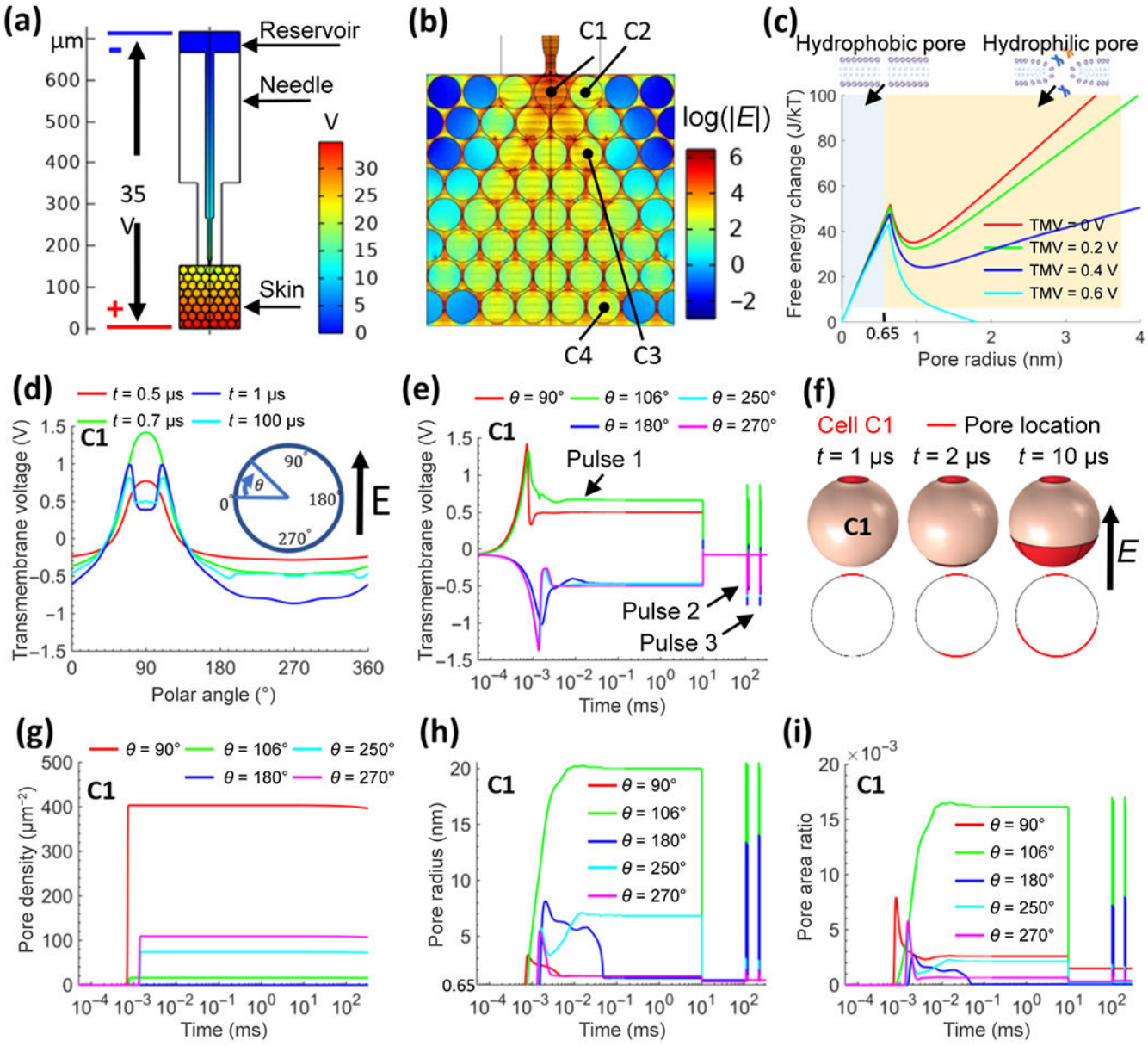

Figure 2.

Simulated results of cell electroporation on tissue. (a) A simplified model of a hollow needle attached on a unit cell of 8 × 7 cell array, applied with 35 V. (b) Electric field (V/mm) distribution throughout the unit cell shown in (a). Cells C1, C2, C3, and C4 are selected for further analysis. (c) Relationship between free energy change and pore radius with different TMV. For cell C1 subject to the electric pulse of 150 V/mm, (d) TMV changes with polar angle at 0.5, 0.7, 1, and 100 μs. (e) TMV changes over time with different polar angles. (f) Pore distribution on the C1 cell at different times shown in three-dimensional (3D) and two-dimensional (2D) views, where (e) represents the direction of the applied electric field. (g) Changes in pore density over time with different polar angles. (h) Evolution of average

pore radius at different polar angles, (i) Pore area ratio changes over time at different polar angles.

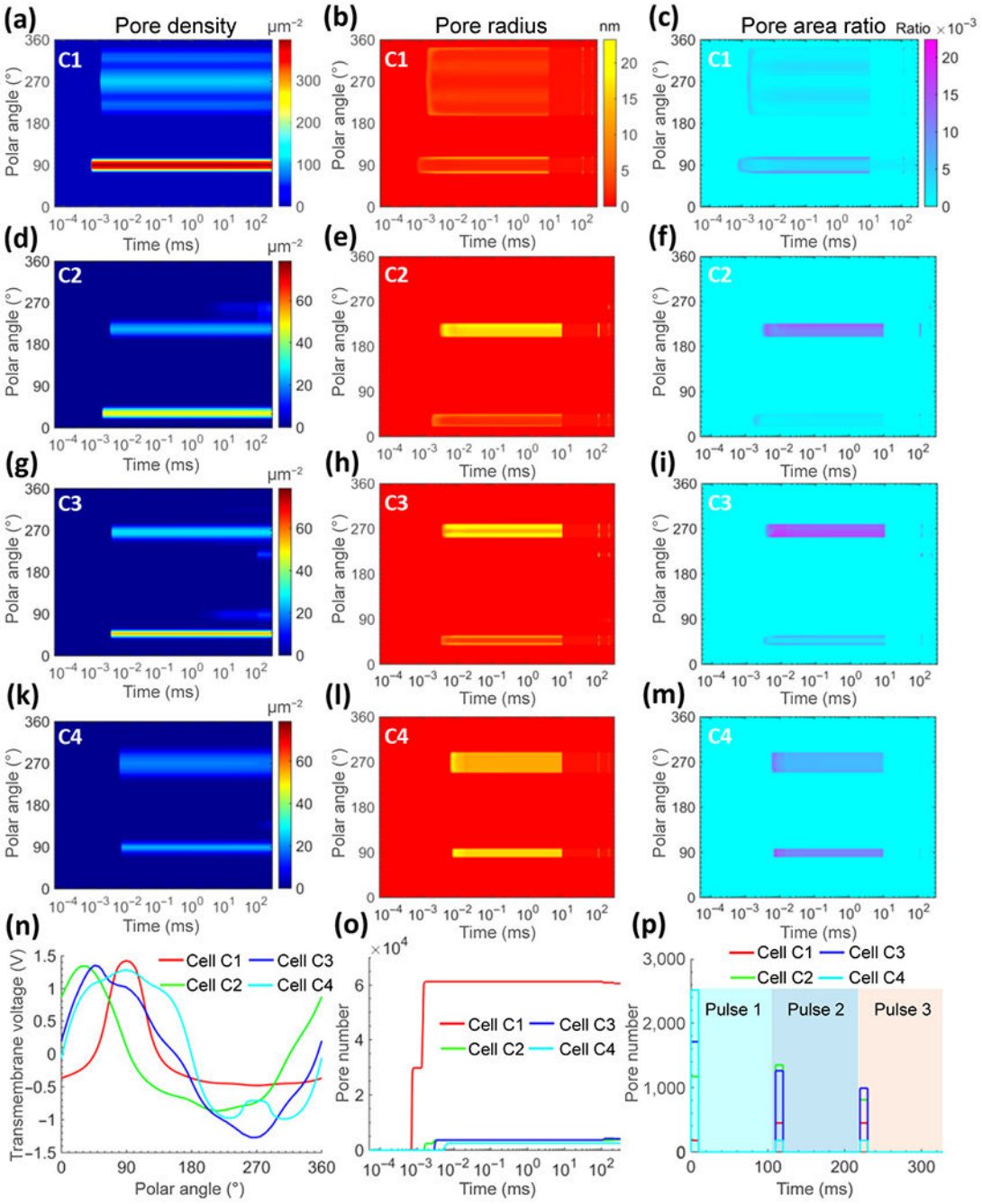

Figure 3.

Comparison of the simulated results among cells C1–C4 at 150 V/mm. (a) Pore density, (b) pore radius, and (c) pore area ratio on the C1 cell membrane over time. Similarly, the simulated results of cells C2, C3, and C4 are shown in (d)–(f), (g)–(i), and (k)–(m), respectively. (n) Comparison of TMV distributions of the cells with polar angles, where the times were chosen for maximum TMV values (C1 at 0.7 μs, C2 at 1.6 μs, C3 at 2.9 μs, C4 at 6.4 μs). (o) Comparison of total pore numbers formed over time. (p) Total number of pores with their radii larger than the critical radius.

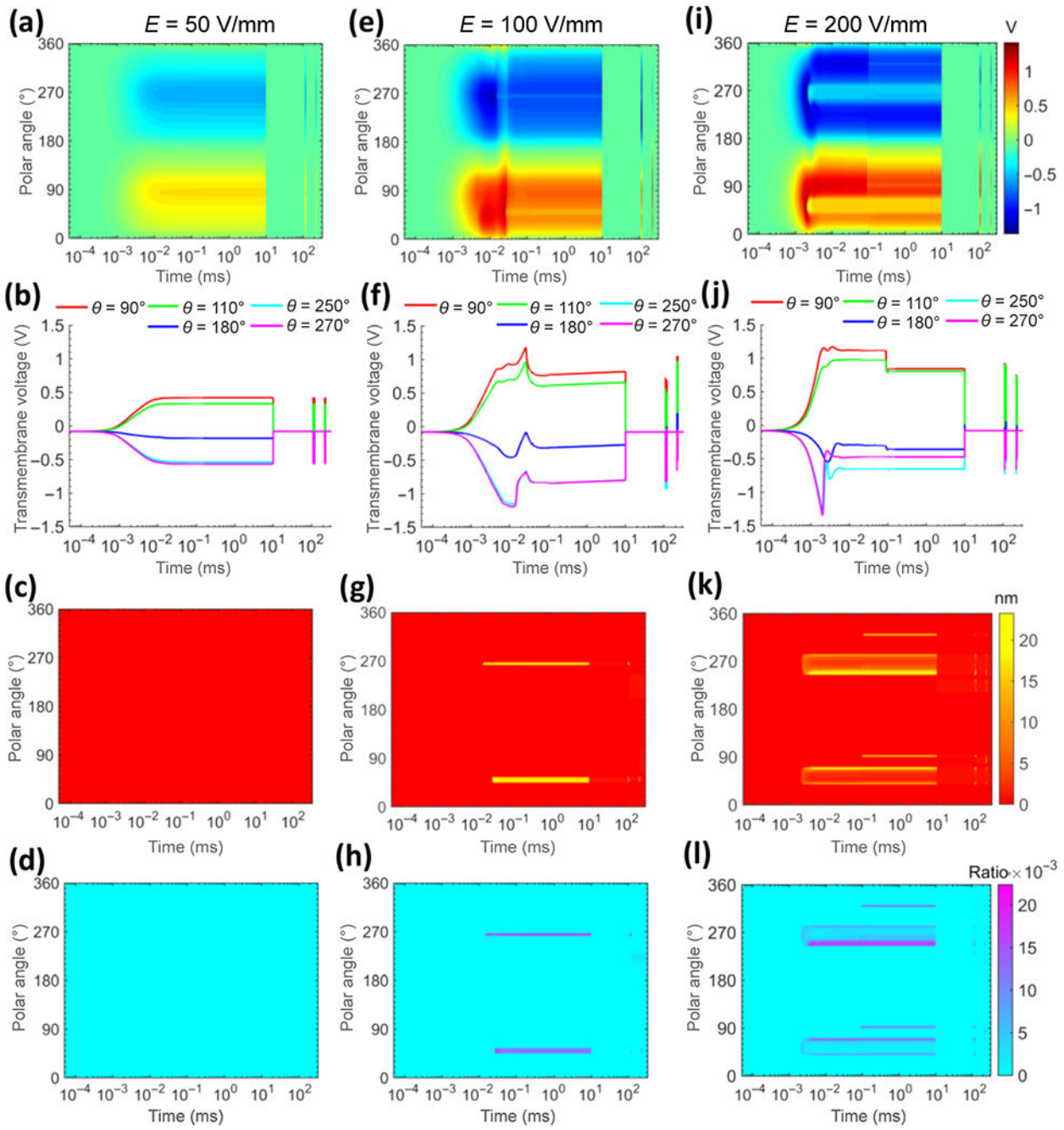

Figure 4.

Tissue electroporation dependence on voltage using C3 cell as an example. (a) TMV distribution under the electric pulse of 50 V/mm. (b) TMV distribution plotted at different polar angles from a. (c) Average pore radius evolution over time. (d) Pore area ratio distribution over time. No pores were created on C3 cell at 50 V/mm, resulting in zero pore area ratio. Similarly, the simulated results under the electric pulse of 100 and 200 V/mm are shown in (e) – (h), and (i) – (l), respectively.

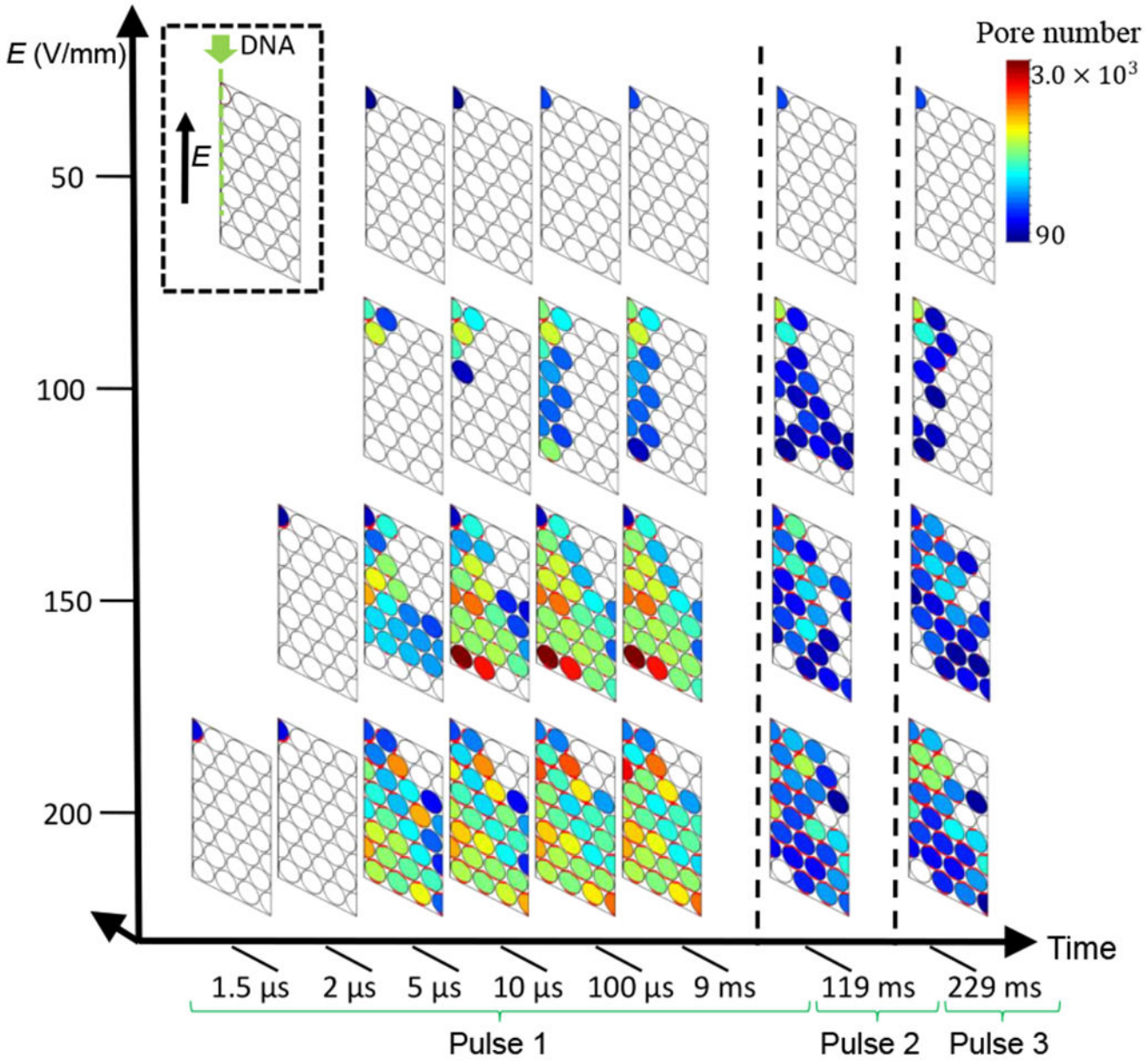

Figure 5.

Pore evolution across the skin tissue at different electric pulses of 50, 100, 150, and 200 V/mm. Only larger pores (> 20 nm) were plotted, and the color represents the pore density. The pulse duration and the interval is 10 and 100 ms, respectively. Half of the unit domain (8 × 3.5 cell array) is shown in this fig. since it is symmetric. The thick red outlines on cells indicate the pores distributions. In order to show the pore evolution, several times are chosen in pulse 1 (1.5, 2, 5, 10, 100 µs, and 9 ms), pulse 2 (119 ms), and pulse 3 (229 ms), respectively.

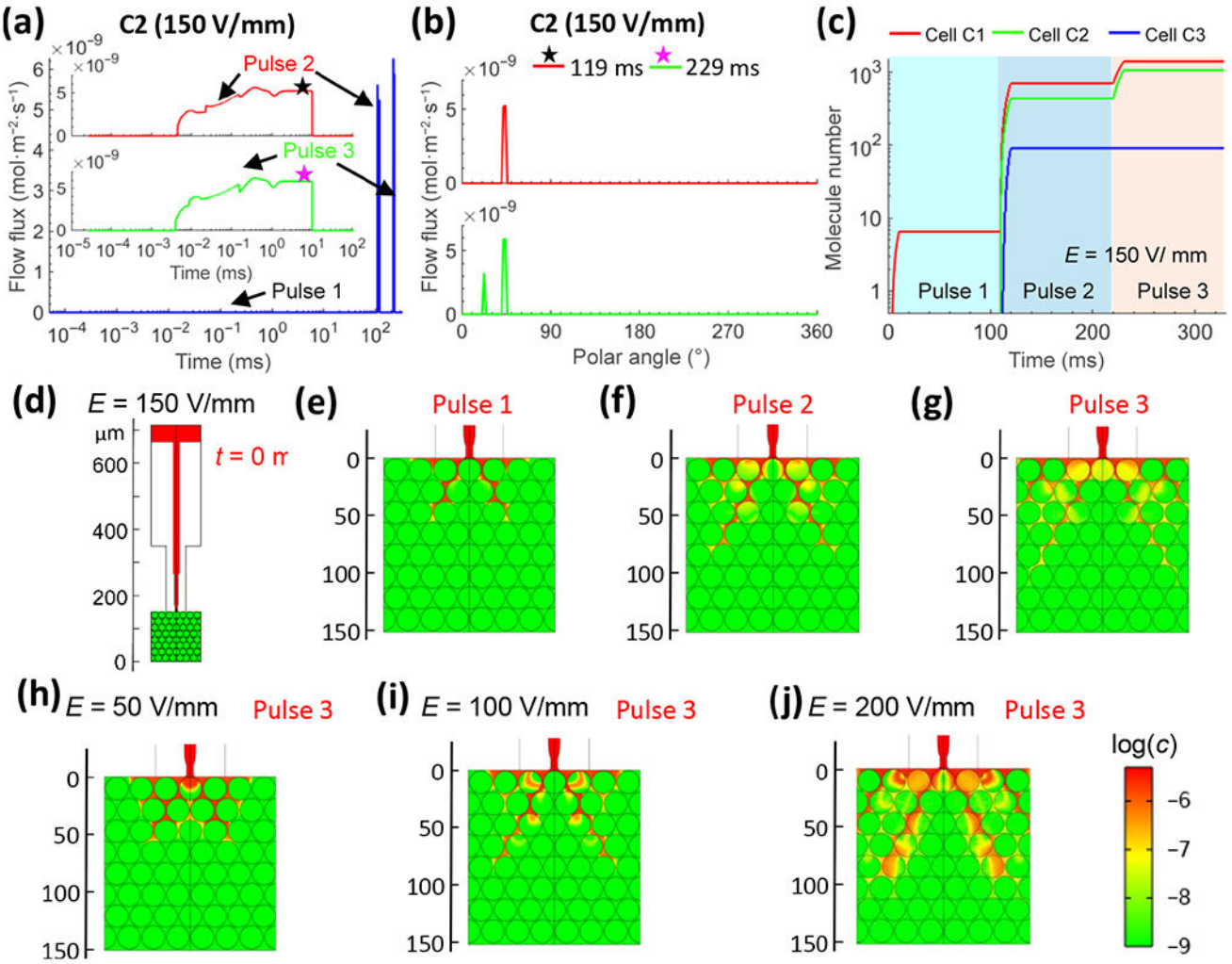

Figure 6.

Simulated results showing plasmid DNA delivery across tissue and entering cells via electrophoresis. (a) DNA flow flux for the cell C2 under the electric pulse of 150 V/mm. (b) DNA flow flux changes with polar angles at 119 ms (pulse 2) and 229 ms (pulse 3). The time positions of 119 and 229 ms are shown in (a) as star marks. (c) The total amount of DNA molecules delivered into the C1, C2, and C3 cells during electric pulses. DNA concentration distribution across the skin structure under the electric pulse of 150 V/mm at before pulse (d), after pulse 1 (e), after pulse 2 (f), and after pulse 3 (g). DNA concentration distribution after 3 pulses under the: electric [ISP]:[ISP]nnkp of 50 (h), 100 (i), and 200 V/mm (j).

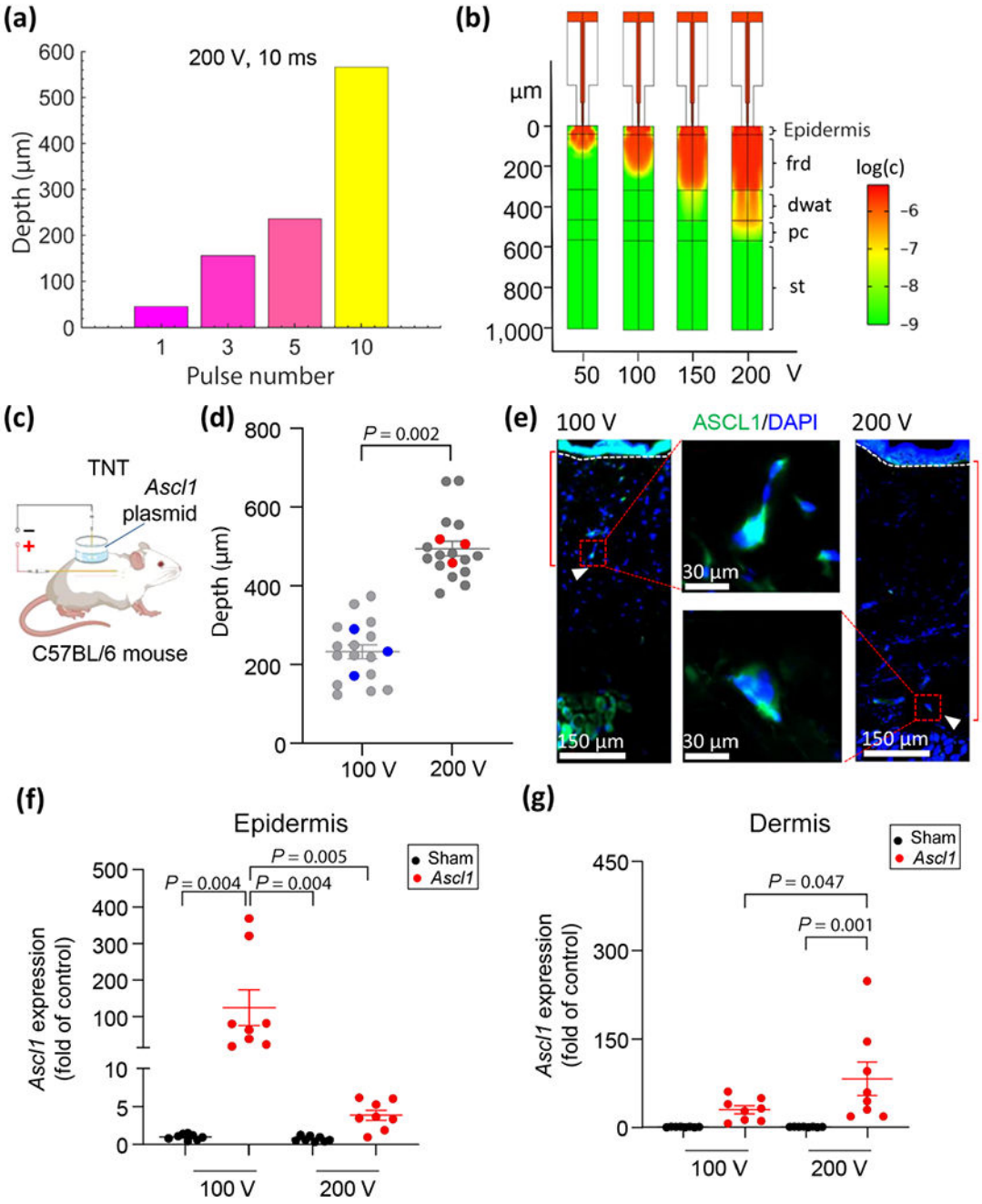

Figure 7.

Simulation and experiment results of plasmid DNA delivery into tissue. (a) Simulated results for delivery depth of plasmid DNA with different pulse numbers under the electric pulse of 200 V/mm. In the simulation of (a), the delivery depth varies with the increase of pulses. (b) Simulation results, (d) and (e) mouse experiment results show delivery depth increase as voltage increases. In the simulation, the skin structure comprises of 5 layers: epidermis, fibroblast rich dermis (frd), dermal white adipose tissue (dwat), panniculus carnosus (pc), and subcutaneous tissues (st). (c) Schematic diagram showing delivery of *Ascl1* plasmid via

TNT in dorsal skin of mouse. (f) and (g) Expression of *Ascl1* plasmid in epidermis (f) and dermis (g) at 100 and 200 V, respectively.